



Cite this: *RSC Adv.*, 2025, 15, 36103

# Cluster expansion-accelerated exploration of the surface structure properties of a PdPtAg ternary alloy for the oxygen reduction reaction across the compositional space

Minghao Hua,<sup>ab</sup> Shuo Li,<sup>c</sup> Xuelei Tian,<sup>\*b</sup> Xiaohang Lin <sup>\*b</sup> and Guoxiang Li<sup>\*a</sup>

A cluster expansion (CE) model was constructed for the ternary alloy Pd/Pt/Ag surface based on density functional theory (DFT) calculations, and Monte Carlo (MC) simulations based on CE were then performed to investigate the surface segregation and atomic ordering on the ternary alloy surfaces at finite temperatures. Results indicated that the local chemical environment of the ternary alloy surface strongly depended on its bulk composition and varied significantly as a function of temperature, producing a significant impact on the catalytic performance. Analysis of depth-resolved composition indicated that even at high temperatures, the dopant metal (Pd or Pt) remained energetically favorable in the bulk, while Ag tended to segregate to the outermost layer to form an enriched layer. DFT calculations indicated that this segregation behavior was driven by the different surface energies between the metals. The Pd concentration exhibited a peak in the second layer and increased with decreasing temperature. Atom ensemble analysis demonstrated that the doped atoms formed a finite number of distinct configurations, with the monomers being the most prevalent surface species. Although surface segregation reduced the number of surface-doped elements, the enrichment of Ag on the surface layer increased the number of unique catalytic active sites on the surface, and the concentration of doped atoms increased by approximately 10% compared with the binary alloy (Pd/Ag or Pt/Ag).

Received 16th July 2025  
Accepted 7th September 2025

DOI: 10.1039/d5ra05089h

rsc.li/rsc-advances

## 1. Introduction

Alloy materials have a wide range of chemical reaction applications in catalysis due to their multifunctional properties.<sup>1,2</sup> The surface composition and corresponding bulk concentration of the alloys usually exhibit certain differences, and phenomena such as surface segregation, reconstruction and ordering may occur. These phenomena can significantly affect the surface structure of alloys and their performance in multiphase and electrochemical processes.<sup>3,4</sup> Specifically, the catalytic activity and selectivity depend on the surface concentration and distribution of the reactive atoms. Many studies focus on specific alloy compositions, such as particular element ratios or chemical ordering, such as intermetallic and core-shell structures. These experimental and theoretical studies, addressing the phenomenon of surface segregation, have used techniques

such as X-ray photoelectron spectroscopy (XPS), Auger electron spectroscopy (AES), low energy electron and diffraction (LEED) to measure the specific surface concentration of alloys.<sup>3,5–8</sup> Conventional high-throughput experimental and computational approaches require an extensive amount of time and resources to effectively explore such expansive design spaces.<sup>9</sup> With the limitations of experimental methods and the development of computational resources, there is a growing need for theoretical studies of surface segregation. Most of the theoretical researches are based on statistical thermodynamics, constant bond energy models, and molecular dynamics and are combined with some simulation methods such as Monte Carlo (MC), but they usually exhibit low accuracy.<sup>10–13</sup> To obtain higher accuracy, density functional theory (DFT) is also employed to calculate the energies of stable alloy configurations but is usually limited to small-scale systems. Furthermore, most theoretical studies focus on bimetallic alloys, with limited work addressing ternary alloys using empirical potentials.<sup>11–15</sup> Although many studies have explored ternary alloys in various contexts, experimental and theoretical studies that explicitly address surface segregation and atomic-scale ordering have predominantly focused on binary systems. Detailed investigations of these phenomena in ternary alloy surfaces remain comparatively limited.<sup>9,16,17</sup> To fully understand the key factors

<sup>a</sup>School of Nuclear Science, Energy and Power Engineering, Shandong University, 250061, Jinan, People's Republic of China. E-mail: liguox@sdu.edu.cn

<sup>b</sup>Key Laboratory for Liquid-Solid Structural Evolution and Processing of Materials, Ministry of Education, School of Materials Science and Engineering, Shandong University, 250061, Jinan, People's Republic of China. E-mail: lxh12345@sdu.edu.cn; tianxuelei@sdu.edu.cn

<sup>c</sup>School of Criminal Science and Technology, Shandong Police College, 250014, Jinan, People's Republic of China



that influence surface segregation, comprehensive research on the alloy composition space is necessary, but such studies are relatively scarce and mostly focus on a specific alloy composition.<sup>18</sup>

The oxygen reduction reaction (ORR) is a critical process in fuel cells and metal–air batteries. Platinum (Pt) is the most active and durable material among ORR catalysts.<sup>19–21</sup> The slow kinetics of ORR necessitate the use of catalysts containing large amounts of Pt-group noble metals to accelerate the reaction. The high cost and scarcity of Pt have driven extensive research efforts to minimize its use.<sup>22</sup> Therefore, designing ORR catalysts with higher activity and lower cost has been a long-standing focus of both academia and industry.<sup>23</sup> In this context, multi-component alloys are particularly promising because their key properties (such as ensemble effect and ligand effect) cannot be replicated in binary alloys. Ternary (and higher order) alloy systems also exhibit significant functional application value as catalyst materials.<sup>24</sup> Many DFT-based theoretical calculations have driven significant progress in screening efficient alloy catalysts.<sup>25–29</sup> Given the limitations revealed by the computational screening of binary alloys, comprehensive studies of the surface chemical ordering distribution in multi-component systems and its impact on catalytic performance are crucial.<sup>30</sup>

The complex interactions in ternary systems make it important to study across the entire compositional space rather than just using a few discrete compositions. Machine learning has emerged as a powerful tool in atomic simulations by enabling efficient surrogate models trained on DFT data. Machine learning models can be trained on DFT-calculated database atomic configurations, and properly trained machine learning models achieve greater computational efficiency than DFT while maintaining comparable accuracy under certain conditions.<sup>15,30–32</sup> Although there are many studies of its use for bimetallic alloys, it has relatively few applications in studies for ternary or multi-component systems such as high-entropy alloys. The machine learning training sets remain constrained in scale, requiring structure datasets of significantly larger orders of magnitude. Recent machine learning studies on ternary and multivariate surface structures have used more than 10 000 bulk structures and 4000 surface structures for training, which remains computationally expensive for the rapid screening of multi-component alloy systems.<sup>33</sup> Based on the screening of PdAg and PtAg alloys with better single atom alloy (SAA) formation capability in previous studies,<sup>34–36</sup> in this work, we investigated the Pd/Pt/Ag(111) ternary alloy surfaces with DFT accuracy. We fitted the cluster expansion (CE) with a low-cost training dataset (266 surface structures), and subsequently explored the Pd/Pt/Ag(111) ternary alloy surfaces across different temperatures and compositional space using MC simulation, aiming to find a superior SAA catalyst to the above bimetallic alloy. The combination of CE + MC promotes a deeper understanding of the structural changes in ternary or multi-component alloy surfaces, significantly reducing computational costs compared to DFT calculations and machine learning models. This provides a feasible method for revealing the characteristic geometric configurations and unique atomic combinations of active sites in multi-component alloy catalysts.

## 2. Computational methods

### 2.1 First-principles calculations

All DFT calculations were performed using the Vienna *Ab initio* Simulation Package (VASP).<sup>37</sup> The projector-augmented wave (PAW) method was employed to describe the interactions between electrons and ions, and the revised Perdew–Burke–Ernzerhof (RPBE) exchange–correlation functional was used to account for electronic interactions.<sup>38,39</sup> The plane-wave cutoff energy was set to 500 eV.<sup>40</sup> All structures were fully relaxed until the energy and force reached the convergence thresholds of  $1 \times 10^{-5}$  eV and  $0.02 \text{ eV } \text{\AA}^{-1}$ , respectively. For structural optimizations of bulk structures, a  $\Gamma$ -centered  $k$ -point mesh of  $25 \times 25 \times 25$  was adopted. The calculated bulk lattice constant of Ag was  $4.21 \text{ \AA}$ , which is in excellent agreement with the experimental value of  $4.09 \text{ \AA}$  and previously reported theoretical values.<sup>41–43</sup>

All surface models were constructed as six-layer slabs of the (111) surface of a face centered cubic (fcc) lattice. To address the complexity of the computational model, the bottom three atomic layers were composed of pure Ag to represent the bulk and were fixed at the corresponding bulk Ag lattice positions. Each site in the other layers can be occupied by one of Pd/Pt/Ag to simulate surface alloys. During the CE fitting process, randomly occupied atomic configurations were generated using the mmaps and gensqs codes in ATAT.<sup>44</sup> Furthermore, all structures with different compositions were fully relaxed during the calculations. A vacuum region of  $20 \text{ \AA}$  was added along the  $z$ -direction to eliminate interactions between periodic images. Surface calculations were performed with dipole correction (IDIPOL = 3) in the direction of the surface normal to achieve faster convergence of the total energy with increasing vacuum thickness and to correct for the electrostatic potential within the vacuum region.<sup>45</sup> For surface structure optimization in the CE training dataset, a  $\Gamma$ -centered  $k$ -points mesh was used for the Brillouin zone integrations. The  $k$ -points per reciprocal atom (KPPRA) value of 2000 was used with  $k$ -points set to 1 in the  $z$ -direction. The  $k$ -point grids were then determined automatically for different alloy configurations by KPPRA and the number of atoms.<sup>44</sup>

The segregation energy ( $\Delta E_{\text{seg}}$ ), which characterizes the preference of dopant atoms to reside on the surface or in the bulk of the alloy, is defined as follows:

$$\Delta E_{\text{seg}} = E_{\text{tot,bulk}} - E_{\text{tot,surf}} \quad (1)$$

Here,  $E_{\text{tot,bulk}}$  is the total DFT energy when the dopant atom is embedded in the third layer of the surface model, and  $E_{\text{tot,surf}}$  is the total energy when the dopant atom resides on the surface layer. A negative value of  $\Delta E_{\text{seg}}$  indicates a preference for the bulk, whereas a positive value suggests a preference for the surface layer.<sup>46,47</sup>

### 2.2 Cluster expansion (CE) and Monte Carlo (MC) simulations

DFT is a well-established technique that is extensively employed to investigate the structures and energies of various materials.



However, determining the configurations of multimetallic alloys involves hundreds or even thousands of atoms, rendering the direct application of DFT both computationally prohibitive and impractical.<sup>48</sup> The cluster expansion method, based on the Ising model, is widely used to calculate the Hamiltonians of different atomic arrangements on a parent lattice.<sup>49,50</sup> In this framework, the system's energy is characterized by the energy corresponding to any atomic distribution on the lattice. The occupation of each spin over the lattice sites of a structure represents configuration  $\sigma$ . The formalism of CE parameterizes the total energy of a structure as a linear combination of interactions between different clusters (eqn (2)).

$$E(\sigma) = \sum_{\alpha} m_{\alpha} J_{\alpha} \prod_{i \in \alpha'} \sigma_i \quad (2)$$

$E(\sigma)$  is the total energy of the system with configuration  $\sigma$ ,  $\alpha$  denotes a particular cluster,  $m_{\alpha}$  is the cluster multiplicity,  $J_{\alpha}$  is the effective cluster interaction (ECI) of that cluster, and  $\langle \dots \rangle$  is the cluster correlation function.<sup>49</sup> The energies of the generated configurations by DFT calculations are collected and fitted to CE models. Although these models are performed on a rigid lattice, atomic relaxations are effectively accounted for in the effective cluster interactions by incorporating relaxed configurations during the fitting process.<sup>35,51</sup> To predict the near-surface atomic segregation and arrangement of the ternary alloy, CE training was performed on Pd/Pt/Ag(111) surfaces. As shown in Fig. 1, all Pd/Pt/Ag(111) surfaces were constructed as six-layer  $2 \times 2$  fcc(111) supercells. In these models, the atomic species in the top three layers could vary randomly, covering concentrations from 0% to 100% to comprehensively sample the entire compositional space. The CE method requires a training dataset of energies for distinct atomic configurations obtained from DFT calculations. Structure generation and CE fitting calculations were conducted using the mmaps code from the Alloy Theoretic Automated Toolkit (ATAT).<sup>52</sup> By sequentially increasing the number of configurations and atomic clusters considered, the final database comprised 266 symmetry-inequivalent surface structures.

The predictive capability of the truncated CE model was assessed by the leave-one-out cross-validation (LOOCV) score, defined as:

$$\text{LOOCV} = \sqrt{\frac{1}{N_s} \sum_i (E_i - \hat{E}_{(i)})^2} \quad (3)$$

where  $N_s$  is the number of structures. For structure  $i$ ,  $E_i$  is the DFT calculated energy and  $\hat{E}_{(i)}$  is the fitted energy predicted by the cluster expansion model built with  $E_i$  excluded from the training set.<sup>53</sup>

Relative to the DFT calculations, the final CE model achieved a LOOCV error of 0.0039 eV, indicating excellent fitting and predictive performance. The ECIs did not change significantly even if more structures from DFT calculations were added. Under these conditions, the cluster expansion energies can be considered highly accurate for calculating or predicting the energy of any given alloy configuration.

To investigate long-range ordering and minimize size effects, each layer of the supercells used in MC simulations contained  $40 \times 40$  atoms, with the dimension along the surface normal set to be equal to that of the surface model illustrated in Fig. 1. MC simulations were performed on the surfaces of 36 different bulk compositions in total as shown in Fig. 2. The atomic ratios reported in the text refer only to the proportion of variable atomic sites; sites with fixed species were excluded from the statistical analysis.

Simulated annealing was carried out using canonical ensemble MC simulations (based on the converged CE), in order to identify the most stable configurations. During the simulations, the number of atoms, cell volume, and temperature ( $NVT$ ) were kept constant. The atomic ratios appearing in the text were only the relative ratios of active sites, while sites with constant species are neglected in the statistics. For each composition (Fig. 2), five independent Monte Carlo annealing runs were started from different random initial configurations to reduce dependence on the initial state and to increase the chance of finding the lowest-energy configuration. The lowest energy configuration found among the five runs was taken as the putative ground state. In each simulation, the initial

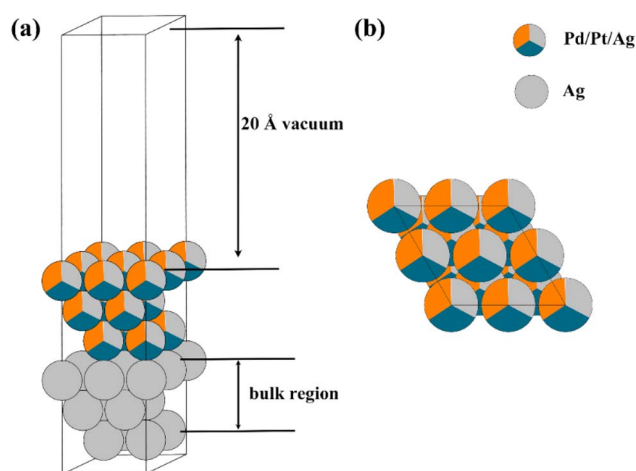


Fig. 1 Surface model used for fitting the cluster expansions and MC simulations. (a) Side view and (b) top view of a  $2 \times 2$  (111) unit cell. The top four surface layers were allowed to be replaced by Pd, Pt or Ag in the surface CE calculations.

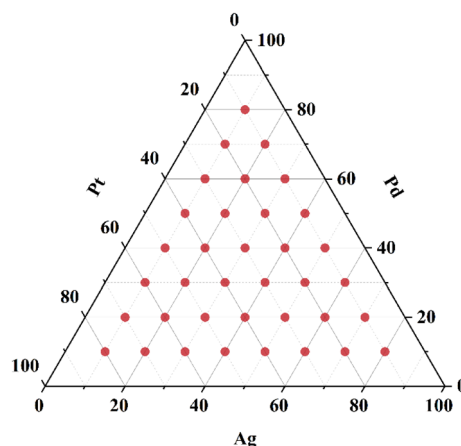


Fig. 2 Bulk concentrations for the MC simulation (red dots).



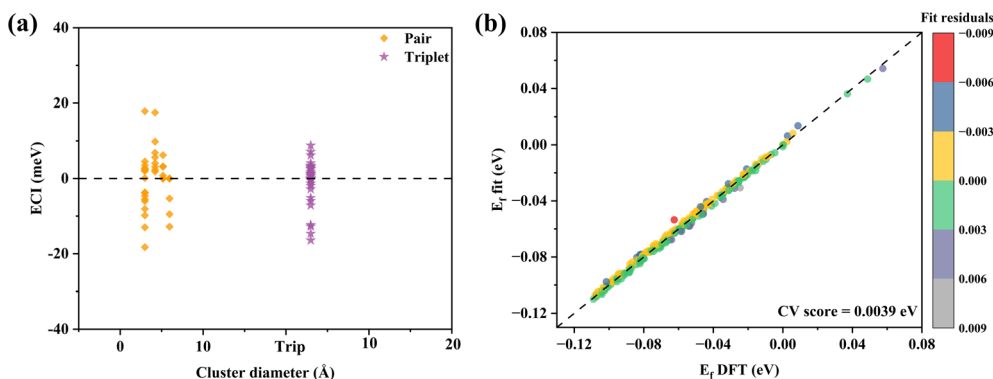


Fig. 3 Cluster expansion results for the Pd/Pt/Ag ternary alloy system. (a) Variation of the clusters and the corresponding ECIs *versus* the interaction distance. (b) Predicted energies using the CE approach *versus* energies obtained using DFT calculations for the Pd/Pt/Ag ternary system, which show the predictive power of the fitted cluster expansion models. The dashed line ( $y = x$ ) indicates the case when the results of the two methods are exactly equal, and the closer the point is to the dashed line, the smaller is the error between the two methods. The different color mappings represent the differential values between DFT energies and CE predicted energies.

configurations were generated at  $T = 100\,000$  K to ensure a random distribution of elements at the outset. The simulations were carried out from a high temperature (3000 K), and gradually decreased to a low temperature (50 K) with a temperature step of 50 K. To ensure adequate sampling of the phase space corresponding to the distribution of alloying elements, multiple MC simulations were conducted on the different initial structures within the canonical ensemble. Equilibrium was reached once the standard deviation of the energy during each MC calculation was less than  $1 \times 10^{-5}$  eV. All MC calculations were performed using memc2 in ATAT.<sup>52</sup>

### 3. Result and discussion

#### 3.1 Validation of the CE models

A total of 266 configurations was generated for the Pd/Pt/Ag ternary alloy surfaces, with the atomic composition of each of the top three layers varying within the range  $[0, 1]$ . The final CE model was obtained through examination of the convergence of the LOOCV score. Typically, the LOOCV score decreases with increasing cluster diameter, and then either increases or remains nearly constant beyond a certain diameter as shown in Fig. 3a, indicating that further inclusion of larger atomic clusters does not improve the predictive capability of the CE model. In the case of Pd/Pt/Ag surfaces, pair clusters play a more significant role. However, their contributions diminish when the diameter exceeds the second nearest neighbor. Short-range three-body clusters are sufficient to reduce the LOOCV score to a very low value of 0.0039 eV, demonstrating excellent accuracy and convergence of the CE fitting. Fig. 3b shows a comparison between the formation energies fitted by CE and those calculated by DFT, indicating good agreement between the two approaches. These results clearly demonstrate the accuracy of the CE method in describing the configuration-dependent surface energies in these ternary alloy systems.

#### 3.2 Tendency of surface segregation

Previous studies on alloy surface segregation have typically relied on comparing the energetic preference of dopant atoms

for occupying the top surface layer *versus* remaining in the bulk.<sup>14,54</sup> Using the developed CE model, we investigated the surface segregation behavior of Pd/Pt/Ag(111) ternary alloys *via* MC simulations at various temperatures, thereby providing more comprehensive information on the surface segregation over a wide compositional range under finite temperature conditions.

Fig. 4 presents MC simulation results at three representative temperatures (2000 K, 1200 K, and 400 K) for 36 bulk concentrations. The excess concentration of element  $i$  is defined as the difference  $\Delta C_i = C_{\text{surf},i} - C_{\text{bulk},i}$ , where  $C_{\text{surf},i}$  is the concentration of element  $i$  in the first layer and  $C_{\text{bulk},i}$  is the concentration of element  $i$  in the active site region (top three layers). Therefore, positive values indicate surface enrichment (*i.e.*, an excess at the surface concentration compared to the bulk), while negative values represent surface depletion. The simulation results demonstrate that, except for the region near the PdPt binary alloy (where Pd segregates to the surface), Pd generally prefers to reside in the bulk at most other compositions, with its surface concentration lower than that in the bulk. For Pt, surface depletion is observed at all bulk concentrations, particularly near the PtAg region. In contrast, Ag consistently segregates to the surface at all bulk concentrations, resulting in strong surface enrichment. These segregation trends show partial consistency with the results previously obtained for binary alloys.<sup>34,35,55</sup>

As shown in Fig. 4a, even at the high temperature of 2000 K, surface segregation still occurs. For instance, at the bulk composition of Pd<sub>10</sub>Pt<sub>40</sub>Ag<sub>50</sub>, the surface Pt concentration in the first layer at 2000 K is only 20.89%, which is 19.11% lower than its 40% value in the bulk concentration, while the Ag surface concentration is enriched by 22.51% compared to its bulk concentration. The surface composition result is consistent with previously reported trends in pure metal (111) surface energies: Ag(111) exhibits the most stable surface energy (0.25 eV per atom on average), followed by Pd(111) at 0.48 eV, with the least stable being Pt(111) at 0.56 eV.<sup>33</sup> Compared to the binary alloy simulations in a previous study, the degree of Ag





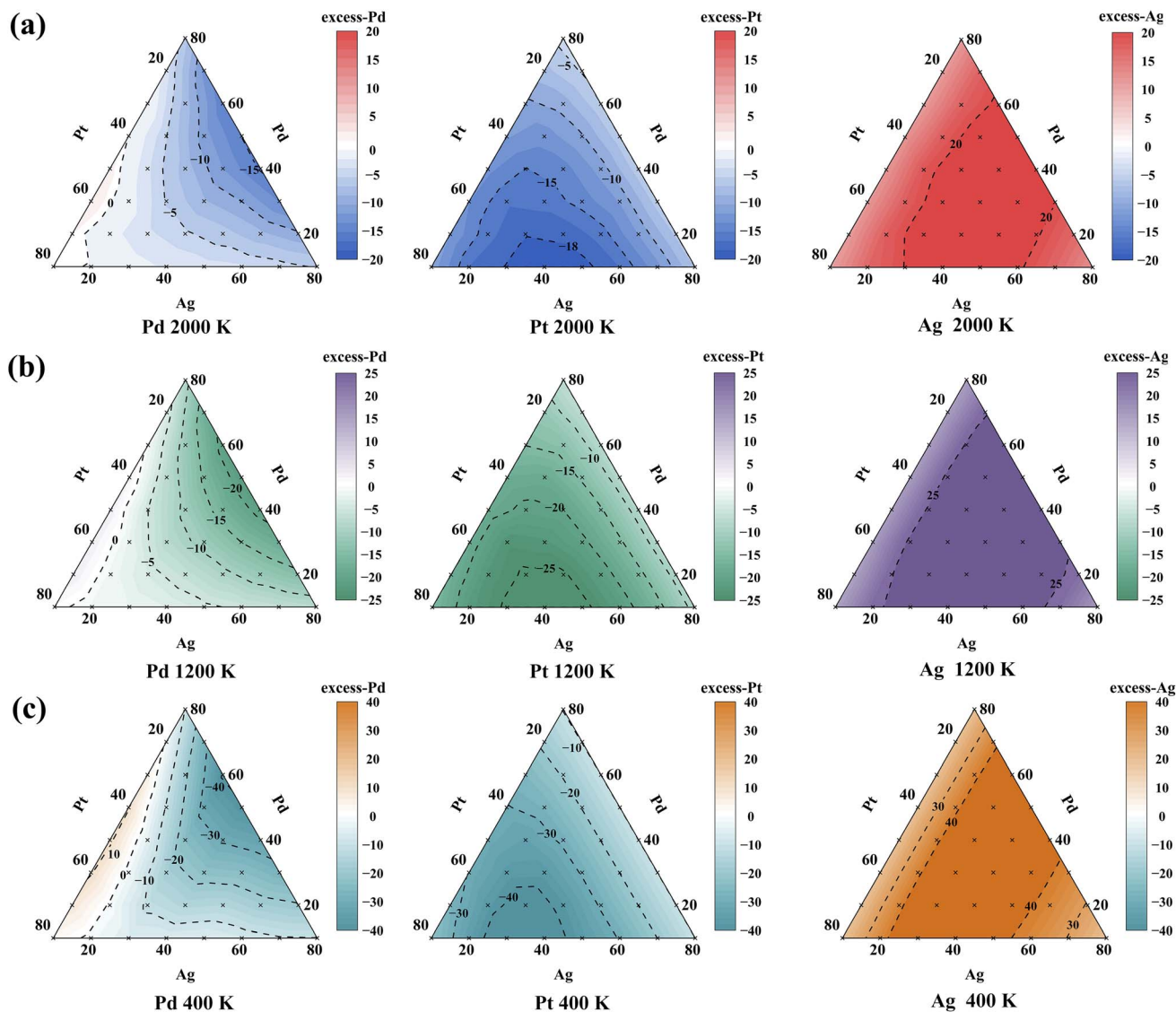


Fig. 4 MC simulation results for surfaces with 36 bulk concentrations at (a) 2000 K, (b) 1200 K, (c) 400 K. These plots show the excess surface composition of the first layer compared to the bulk composition for Pd, Pt, and Ag.

enrichment in the first surface layer is reduced. For binary PtAg and PdAg alloys with 50% Ag in the bulk concentration, the Ag concentration in the first surface layer at 1200 K approaches 90%.<sup>35</sup> In contrast, Fig. 4b shows that for all ternary alloys with 50% Ag bulk concentration, the excess segregation of Ag on the surface is about 30%, corresponding to roughly 80% Ag concentration in the first layer. This indicates that the incorporation of two active metals, Pd and Pt, into the Ag matrix reduces the enrichment of Ag in the surface layer of the ternary alloy, resulting in a higher proportion of active atoms at the surface. At 400 K, Pd segregates to the surface at the bulk composition close to the PdPt binary alloy, with a maximum enrichment of about 10%. Furthermore, as shown in Fig. 4c, lowering the temperature from 2000 K to 300 K intensifies the segregation trends for all elements: for example, the enrichment of the excess concentration of Ag increases from 20% to 40%. The Pd/Pt/Ag ternary alloy surface displays a complex

composition relationship, in which the moderate reduction of Ag enrichment leads to an increased number of unique active sites on the first layer.

To reduce costs and enhance the utilization of noble metals, we aim to reduce the content of noble metals in the catalyst while maximizing the number of active atomic sites on the surface. Consequently, our analysis focuses on ternary alloy surfaces with Ag bulk concentrations in the range of 50–70%. Alloys containing 80% and less than 50% Ag were excluded from consideration due to the insufficient number of active atoms on their surfaces. Detailed statistical results (Fig. S1–S4) for these alloy surfaces are provided in the SI.

Fig. 5 illustrates the statistical results of each element concentration variation in the first and second surface layers for nine selected (50–70% Ag bulk concentration) ternary alloy surfaces as functions of temperature. Even at the high temperature of 2000 K, strong segregation persists in the first



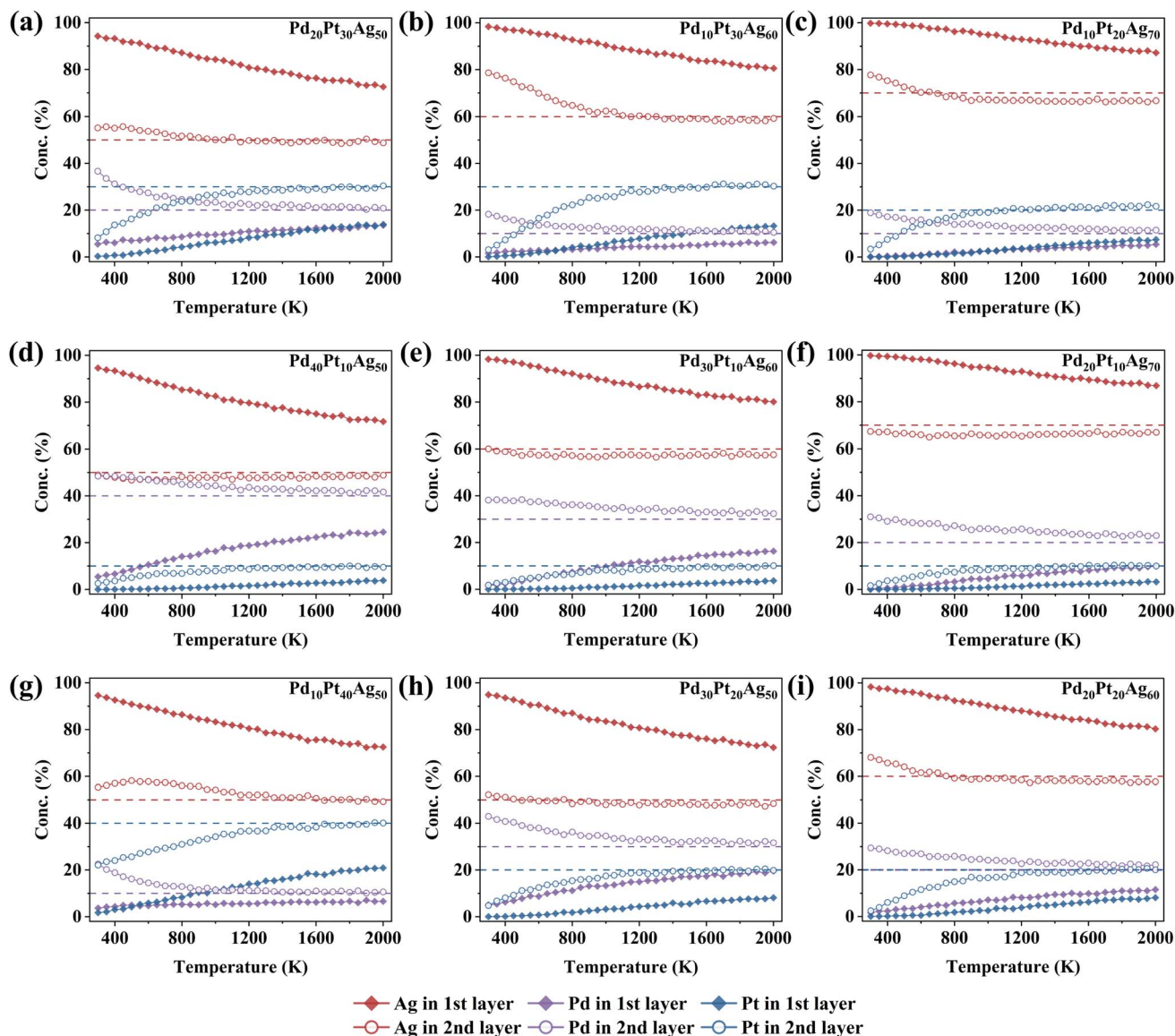


Fig. 5 Average percentage of various atoms in the top two layers at several levels of typical compositions and temperatures. (a)  $\text{Pd}_{20}\text{Pt}_{30}\text{Ag}_{50}$ , (b)  $\text{Pd}_{10}\text{Pt}_{30}\text{Ag}_{60}$ , (c)  $\text{Pd}_{10}\text{Pt}_{20}\text{Ag}_{70}$ , (d)  $\text{Pd}_{40}\text{Pt}_{10}\text{Ag}_{50}$ , (e)  $\text{Pd}_{30}\text{Pt}_{10}\text{Ag}_{60}$ , (f)  $\text{Pd}_{20}\text{Pt}_{10}\text{Ag}_{70}$ , (g)  $\text{Pd}_{10}\text{Pt}_{50}\text{Ag}_{50}$ , (h)  $\text{Pd}_{30}\text{Pt}_{20}\text{Ag}_{50}$ , and (i)  $\text{Pd}_{20}\text{Pt}_{20}\text{Ag}_{60}$ .

surface layer, while the elemental concentrations in the second layer (represented by hollow circles in different colors in the figure) are close to those in the corresponding bulk compositions. At temperatures around 1200 K, the concentrations of each element in the second layer still remain close to the bulk values, deviating only at lower temperatures below 800 K. This behavior differs from that observed in the  $\text{PdAg}$  and  $\text{PtAg}$  binary alloys, where enrichment of the dopant element in the second surface layer commences at 1200 K. At 300 K and 50% Ag bulk composition, the second layer of the (111) surfaces in both binary alloys shows a dopant enrichment degree of 20–25%.<sup>34,35</sup> In contrast, for the  $\text{PdPtAg}$  ternary alloys, both the extent and onset temperature of Pd enrichment in the second layer are reduced significantly, with deviations from bulk composition only becoming apparent below 800 K. Interestingly, the behavior of Pt in the second layer is fully reversed in the ternary

alloy: starting from temperatures below 1200 K, the concentration of Pt in the second layer decreases and falls below the bulk value. The reduced segregation of dopant elements in the second layer may be attributed to the averaging effect of interactions among the three different atomic species, which weakens the attraction of the Ag-rich first surface layer to the dopant atoms in the subsurface layer.

The trends in the elemental distribution within the first surface layer remain stable across varying bulk compositions. As the temperature decreases from 2000 K to 300 K, the Ag enrichment in the first layer gradually intensifies, resulting in an almost pure Ag surface layer at 300 K, with Pd and Pt concentrations in the first layer concomitantly declining as the temperature drops. The compositional evolution of dopant elements in the second layer is consistent throughout the cooling process: Pd enrichment increases while Pt decreases



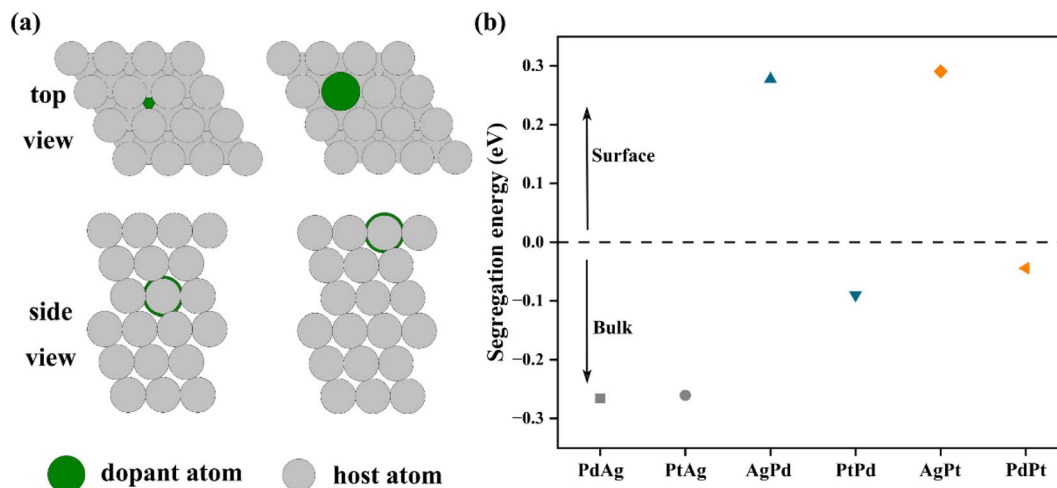


Fig. 6 (a) First row: top view of the (111) slab with the dopant atom (green) being immersed in the third layer of the host matrix (grey, top-left inset), and then being placed on the top layer (top-right inset). Second row: side view of the same slabs. (b) Segregation energies of each slab. We placed the dopant element first and then the host metal for representation. For example, isolated Pd atom sites in a Pt host would be referred to as a PdPt slab.

with decreasing temperature. However, the degree of enrichment for a given element shows unconventional changes as a function of the bulk composition. Typically, an increase in the bulk Pd content would be expected to enhance the Pd enrichment in the second layer. Yet, at 300 K, where segregation is the most pronounced (Fig. 5d–i), the degree of Pd enrichment in the second layer for all these compositions is around 10%, with Fig. 5a and c showing Pd enrichment values close to 15%. Notably, for the  $\text{Pd}_{20}\text{Pt}_{30}\text{Ag}_{50}$  alloy (Fig. 5b), Pd enrichment in the second layer is 22.65% above its bulk concentration, much higher than the 9.55% observed for the  $\text{Pd}_{40}\text{Pt}_{10}\text{Ag}_{50}$  alloy. Such intriguing surface behaviors across compositional ranges at different temperatures are challenging to capture or predict using DFT-based methods, which underscores the advantages and necessity of our CE + MC simulations.

To quantitatively evaluate the segregation tendency of Pd, Pt, and Ag, the segregation energy of each binary pair was calculated by considering each elemental pair in equilibrium within the structure.<sup>46,56</sup> According to eqn (1), a positive segregation energy indicates a thermodynamic tendency for the dopant atom to segregate to the surface, favoring the formation of the SAA structure. Conversely, a negative segregation energy indicates a tendency for immersion of the dopant atom into the host metal matrix. Calculation of segregation energies requires two separate (111) surface computations for each binary alloy: first, with a single dopant atom in the outermost surface layer, corresponding to a SAA structure, and second, with the dopant atom placed in the third layer to simulate the bulk environment within the host metal (Fig. 6a). It should be noted that these calculations provide information about the thermodynamic stability of the various structures, but neglect entropic and kinetic effects. Six distinct (111) surface structures were computed, with the results summarized in Fig. 6b. We find that segregation energies are negative when Ag acts as a host, while they are positive when Ag is the dopant. For Pd/Pt(111) and Pt/

Pd(111), the computed segregation energies are small and negative,  $-0.04$  eV and  $-0.09$  eV, respectively, consistent with the similar surface energies of Pd and Pt atoms on (111) surfaces. In Ag-based alloys, both Pd and Pt dopants have similar segregation energies (close to  $-0.26$  eV), indicating a strong tendency to reside in the bulk and similar levels of segregation. The calculated segregation trends are consistent with those from the CE + MC simulations; however, the MC results for Pd and Pt show differing degrees of segregation for these dopant atoms. This suggests that, for a realistic description of alloy surface segregation at finite temperatures, it is essential to include entropic effects.

### 3.3 Distribution of the tendency of the atomic ensembles for surface segregation

Next, we analyzed the average numbers of monomers, dimers, and multimers of dopant elements in the first surface layer for the different alloy systems shown in Fig. 5. The corresponding statistical results are presented in Fig. 7, with additional data for other bulk concentrations (Fig. S5–S7) provided in the SI (on the surfaces of alloys containing 10% Ag, only multimers are observed, with no monomers or dimers present). Within the range of bulk concentrations and temperatures considered in Fig. 7, the quantity of monomers is significantly higher—by as much as three to four times—than that of dimers and multimers. As the temperature decreases, both dimer and multimer numbers show a declining trend, which is related to the reduced surface concentration of dopant elements at lower temperatures. This indicates that, even in ternary alloys, the PdPtAg systems retain some of the trends observed in binary alloys and maintain a considerable capacity for SAA formation. However, the trend in the number of surface monomers is different. For PdAg alloys, both the number of surface monomers and the surface Pd concentration exhibit a monotonic decrease with decreasing temperature.<sup>35</sup> In contrast, as seen in





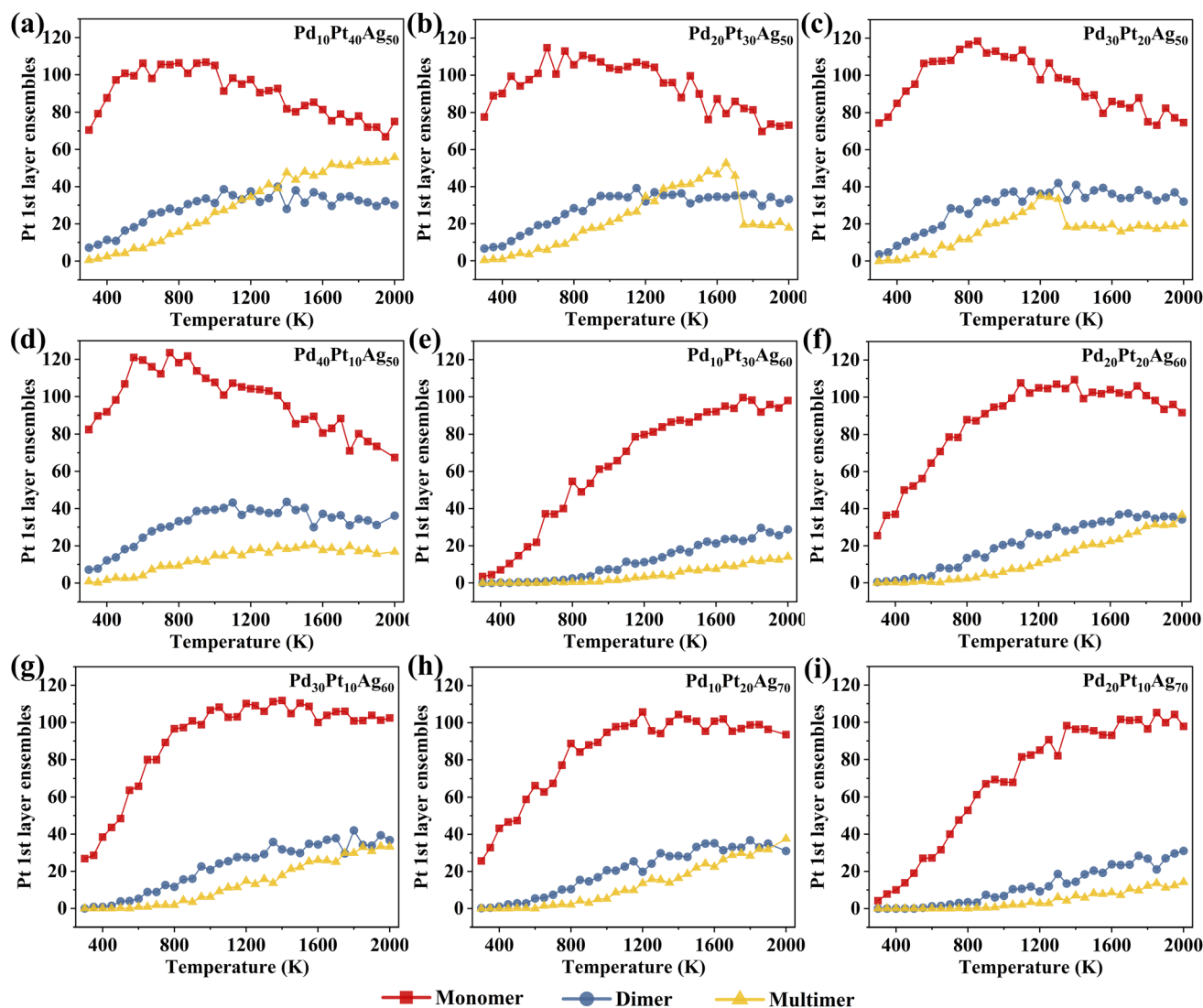


Fig. 7 Statistics of the number of different ensembles (monomers, dimers and multimers) of active dopant atoms in the first layer by MC simulations for different bulk concentrations: (a)  $\text{Pd}_{10}\text{Pt}_{40}\text{Ag}_{50}$ , (b)  $\text{Pd}_{20}\text{Pt}_{30}\text{Ag}_{50}$ , (c)  $\text{Pd}_{30}\text{Pt}_{20}\text{Ag}_{50}$ , (d)  $\text{Pd}_{40}\text{Pt}_{10}\text{Ag}_{50}$ , (e)  $\text{Pd}_{10}\text{Pt}_{30}\text{Ag}_{60}$ , (f)  $\text{Pd}_{20}\text{Pt}_{20}\text{Ag}_{60}$ , (g)  $\text{Pd}_{30}\text{Pt}_{10}\text{Ag}_{60}$ , (h)  $\text{Pd}_{10}\text{Pt}_{20}\text{Ag}_{70}$ , and (i)  $\text{Pd}_{20}\text{Pt}_{10}\text{Ag}_{70}$ .

Fig. 7, ternary alloys display distinct characteristics in the interplay between the monomer number, bulk composition, and temperature.

Specifically, when the Ag bulk concentration is 50% (Fig. 7a–d), the number of monomers initially increases and then decreases with decreasing temperature. Interestingly, regardless of the elemental ratios, the monomer number peaks for these four alloy compositions all occur around 800 K, with the maxima ( $\sim 120$ ) observed in  $\text{Pd}_{30}\text{Pt}_{20}\text{Ag}_{50}$  and  $\text{Pd}_{40}\text{Pt}_{10}\text{Ag}_{50}$ . For Ag bulk concentrations of 60% and 70%, the number of monomers decreases with decreasing temperature, similar to the trend in binary alloys. However, for some compositions (Fig. 7f–h), the monomer number exhibits a plateau between 2000 K and 1200 K, with a pronounced decrease only below 1200 K. Regardless of the specific composition, the maximum monomer number in Fig. 7e–i is about 100. The temperature at which the monomer number peaks varies with the composition

is as follows:  $\text{Pd}_{10}\text{Pt}_{30}\text{Ag}_{60}$  and  $\text{Pd}_{20}\text{Pt}_{10}\text{Ag}_{70}$  show maxima at 2000 K, while  $\text{Pd}_{20}\text{Pt}_{20}\text{Ag}_{60}$ ,  $\text{Pd}_{30}\text{Pt}_{10}\text{Ag}_{60}$ , and  $\text{Pd}_{10}\text{Pt}_{20}\text{Ag}_{70}$  reach their peak values in the range of 1200–1600 K. These results suggest that although the total surface concentration of dopant elements in the first layer monotonically decreases with decreasing temperature (as shown in Fig. 5), the number of surface monomers is jointly influenced by both elemental ratios and temperature, resulting in distinct variation characteristics. Due to the influence of inter-element interactions, the distribution patterns of atomic ensembles observed in binary alloys do not fully translate to ternary alloys.

To investigate the distribution characteristics of atomic ensembles in the surface layer, we selected the surface structures with the highest number of monomers for each Ag bulk concentration (50%, 60%, 70%) for further analysis. Fig. S8 displays structural snapshots of the first surface layer of the  $\text{Pd}_{40}\text{Pt}_{10}\text{Ag}_{50}$  system at various temperatures. At 2000 K, a large





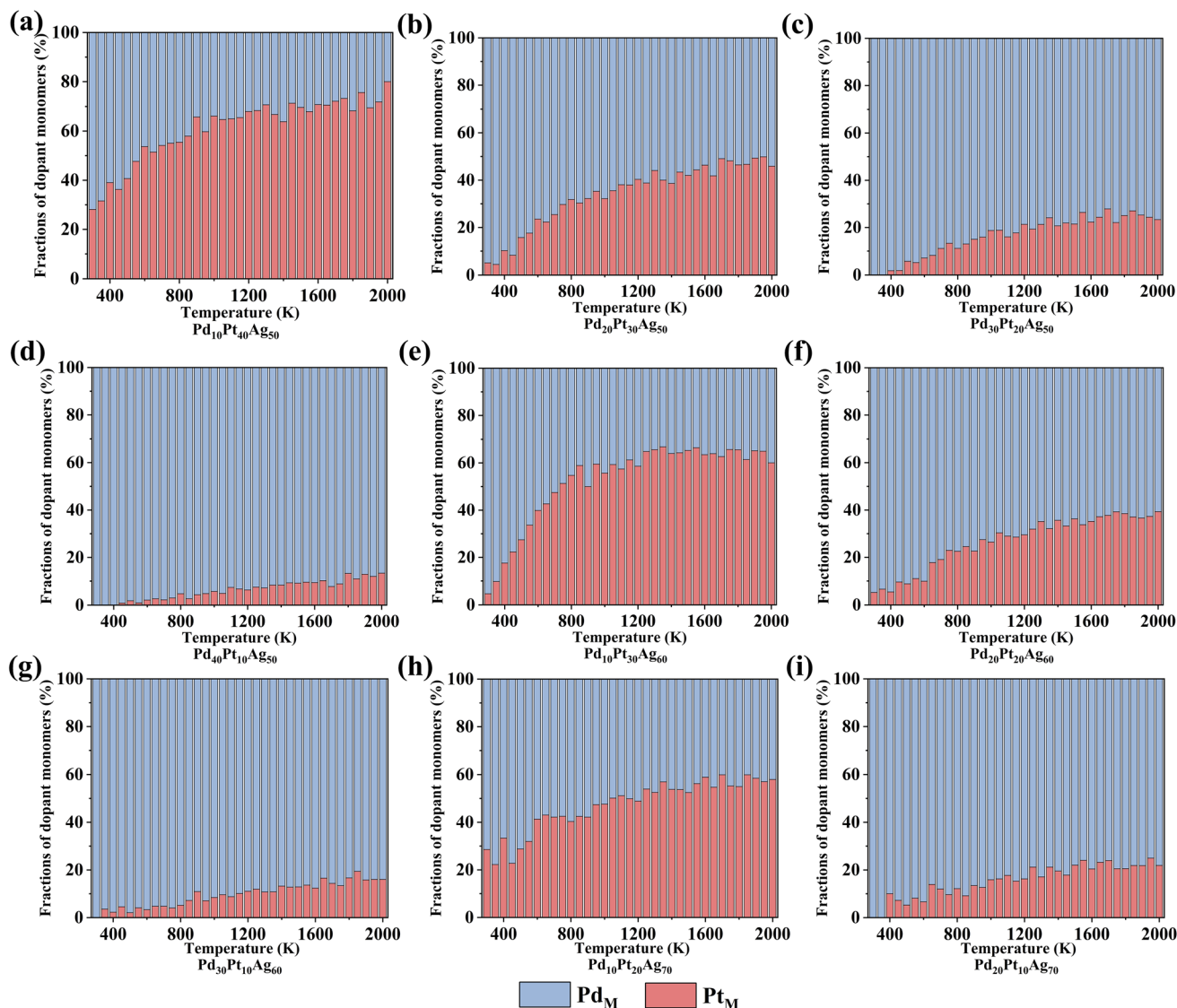


Fig. 8 Element fractions of the monomers of the dopant atoms in the first layer by MC simulations for different bulk concentrations: (a)  $\text{Pd}_{10}\text{Pt}_{40}\text{Ag}_{50}$ , (b)  $\text{Pd}_{20}\text{Pt}_{30}\text{Ag}_{50}$ , (c)  $\text{Pd}_{30}\text{Pt}_{20}\text{Ag}_{50}$ , (d)  $\text{Pd}_{40}\text{Pt}_{10}\text{Ag}_{50}$ , (e)  $\text{Pd}_{10}\text{Pt}_{30}\text{Ag}_{60}$ , (f)  $\text{Pd}_{20}\text{Pt}_{20}\text{Ag}_{60}$ , (g)  $\text{Pd}_{30}\text{Pt}_{10}\text{Ag}_{60}$ , (h)  $\text{Pd}_{10}\text{Pt}_{20}\text{Ag}_{70}$ , and (i)  $\text{Pd}_{20}\text{Pt}_{10}\text{Ag}_{70}$ .

number of dopant atoms remain on the surface, resulting in higher numbers of dimers and multimers, with a significant presence of Pt atoms. At 1200 K and 800 K, abundant monomers are observed on the surface, while the number of multimers decreases from 34 to 9, indicating a notable effect of temperature on the aggregation of dopant elements. When the temperature drops to 300 K, no multimers are present on the surface, and Pt atoms have completely disappeared. As the temperature decreases, the initially high abundance of Pd and Pt atoms on the surface in Fig. S8a is gradually reduced, until only Pd atoms remain in Fig. S8d. This is related to the relatively high instability of the Pt(111) surface energy. The distribution trends are similar in  $\text{Pd}_{30}\text{Pt}_{10}\text{Ag}_{60}$  (Fig. S9) and  $\text{Pd}_{20}\text{Pt}_{10}\text{Ag}_{70}$  (Fig. S10). With increasing Ag bulk concentration, the number of surface monomers at 300 K sharply decreases, by up to a factor of 16. Due to the overall reduction in the number of

dopant atoms, the quantities of dimers and multimers at all temperatures are lower than those observed for the 50% Ag bulk concentration. Similar to the binary alloy case, the distribution of atomic ensembles of different sizes shows disordered characteristics, and no ordered surface structures are observed.

Unlike binary alloys, the Pd/Pt/Ag ternary alloys feature two dopant elements, Pd and Pt. As previously shown, these two dopants exhibit different tendencies for surface segregation; therefore, we performed a statistical analysis of the Pd and Pt proportions in the different atomic ensembles formed on the surface. Fig. 8 presents the elemental proportions in surface monomer ensembles for Ag bulk concentrations ranging from 50% to 70%. Statistical results for other compositions (Fig. S13–S16) are provided in the SI. As shown in Fig. 8a, when the bulk concentration of Pt far exceeds that of Pd, the proportion of Pt among monomers at high temperature is close to its bulk



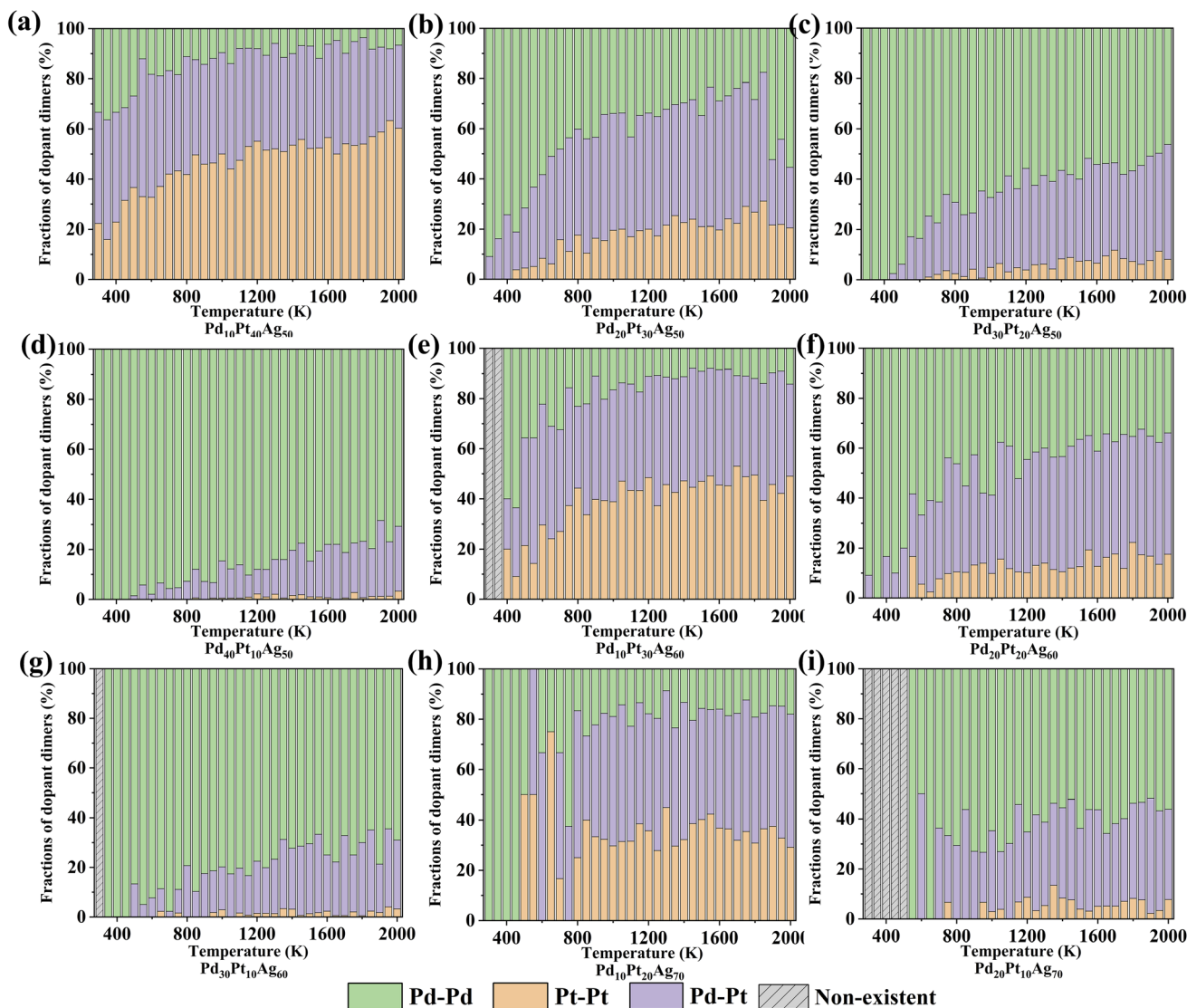


Fig. 9 Fractions of the dimers of the dopant atoms with different coordinations in the first layer by MC simulations for different bulk concentrations: (a)  $\text{Pd}_{10}\text{Pt}_{40}\text{Ag}_{50}$ , (b)  $\text{Pd}_{20}\text{Pt}_{30}\text{Ag}_{50}$ , (c)  $\text{Pd}_{30}\text{Pt}_{20}\text{Ag}_{50}$ , (d)  $\text{Pd}_{40}\text{Pt}_{10}\text{Ag}_{50}$ , (e)  $\text{Pd}_{10}\text{Pt}_{30}\text{Ag}_{60}$ , (f)  $\text{Pd}_{20}\text{Pt}_{20}\text{Ag}_{60}$ , (g)  $\text{Pd}_{30}\text{Pt}_{10}\text{Ag}_{60}$ , (h)  $\text{Pd}_{10}\text{Pt}_{20}\text{Ag}_{70}$ , and (i)  $\text{Pd}_{20}\text{Pt}_{10}\text{Ag}_{70}$ . The gray bars in the figures represent the absence of dimers formed by dopant elements in the first layer under this condition.

fraction. Conversely, when the Pt content is lower than that of Pd, the proportion of Pt in surface monomers is much lower than the bulk Pt content even at high temperature. For example, in Fig. 8c, where the bulk ratio is  $\text{Pd}:\text{Pt} = 3:2$ , the monomer ratio at high temperature is about 4 : 1. For all surfaces, the Pt proportion in monomers decreases as the temperature decreases. Similar to the changing trend in the total number of monomers shown in Fig. 7, the elemental proportions among monomers remain relatively constant between 2000 K and 1200 K, but decrease sharply for Pt below 800 K. Consistent with the atomic structural images in Fig. S10, at 300 K, only Pd atoms remain as monomers on the surface except for  $\text{Pd}_{10}\text{Pt}_{40}\text{Ag}_{50}$ .

We also performed a statistical analysis of the proportions of dimer configurations on the surfaces of systems with Ag bulk concentrations from 50% to 70%, as illustrated in Fig. 9. It can be seen that the number of different dimer types is closely

related to the bulk composition of the dopant elements. In Fig. 9a, for  $\text{Pd}_{10}\text{Pt}_{40}\text{Ag}_{50}$ , the proportion of Pt–Pt dimers exceeds 50% at 2000–1200 K, but drops below 20% at temperatures below 400 K. For the  $\text{Pd}_{40}\text{Pt}_{10}\text{Ag}_{50}$  surface (Fig. 9d), Pd–Pd dimers overwhelmingly dominate at all temperatures, and Pt–Pt dimers account for at most 3.3% (at 2000 K), dropping to less than 1% below 1200 K. Although the bulk Pt content is low, a certain fraction of Pd–Pt dimers persists until the temperature drops to 450 K, at which point they are completely absent. A similar trend is observed in the  $\text{Pd}_{30}\text{Pt}_{10}\text{Ag}_{60}$  and  $\text{Pd}_{20}\text{Pt}_{10}\text{Ag}_{70}$  alloys. For the  $\text{Pd}_{20}\text{Pt}_{20}\text{Ag}_{60}$  surface in Fig. 9f, Pd–Pt dimers constitute the majority in the 2000–1200 K interval, followed by Pd–Pd dimers. As the temperature further decreases, the surface Pt atoms become fewer, leading to a decrease in the fractions of both Pt–Pt and Pd–Pt dimers. Even at 600 K, Pd–Pt dimers still represent 27.8% of the total. Except for Fig. 9a, Pd–



Pd dimers account for more than 50% of dimers on all other surfaces below 600 K, and reach as high as 90–100% below 400 K. This is primarily due to the dramatic loss of Pt atoms from the surface at low temperatures. Overall, Pd and Pt dopants show a certain degree of mutual attraction on the Ag-hosted surface, resulting in a non-negligible proportion of Pd–Pt dimers. However, this heteroatomic attraction is limited, leaving a majority of Pd–Pd dimers and a minority of Pt–Pt dimers on the surface. The presence of Pt on the surface is another crucial factor affecting the distribution of different dimer species. Such large-scale surface segregation and atomic aggregation information is unattainable using only DFT calculations; in contrast, the CE + MC approach allows for global or even exhaustive searches of the alloy surface phase space as a function of both composition and temperature, enabling the prediction of the surface atomic structure.

## 4. Conclusion

In this study, we constructed cluster expansion (CE) models for the Pd/Pt/Ag(111) ternary alloy surfaces based on DFT calculations, and utilized these models to perform Monte Carlo (MC) simulations in order to investigate surface segregation and atomic ordering at finite temperatures. The results reveal that the local chemical environment at the alloy surface strongly depends on the bulk composition and exhibits considerable fluctuations with changing temperature, which may have significant implications for the catalytic performance of alloy surfaces. Composition analysis of atomic layers at different depths indicates that, even at high temperatures, the dopant metals (Pd or Pt) tend to remain in the bulk, while Ag preferentially forms an enriched layer at the topmost surface. DFT calculations demonstrate that this segregation behavior originates from differences in the surface energies of the pure metals. The concentration of Pd peaks in the subsurface layer and increases as the temperature decreases. Unlike the consistent trend between the surface monomer number and the peak temperature observed for binary alloy surfaces, the PdPtAg ternary alloy surface displays a more complex, diversified relationship. Although surface segregation leads to a reduction in the number of dopant atoms at the surface, the enrichment of Ag increases the number of unique catalytically active sites on the surface, and the concentration of dopant atoms on the topmost layer is approximately 10% higher than that in binary SAAs. The results suggest that surface segregation at finite temperatures and the resulting changes in the surface atomic structure must be fully considered in catalyst composition optimization and surface design. The combination of CE and MC thus facilitates an in-depth understanding of the structural evolution at ternary or multicomponent alloy surfaces, providing a feasible approach to reveal the characteristic geometric configurations and unique atomic ensemble active sites of multicomponent single-atom alloy catalysts.

## Conflicts of interest

The authors have no conflicts to disclose.

## Data availability

The full dataset of the 266 surface structures is available on GitHub at <https://github.com/Huamh/Data-for-cluster-expansion-of-PdPtAg-ternary-alloy>.

The data supporting this article have been included as part of the SI. Supplementary information: the additional statistical results of atomic ensembles for different concentrations. See DOI: <https://doi.org/10.1039/d5ra05089h>.

## Acknowledgements

This work was supported by the Shandong Provincial Natural Science Foundation (ZR2024QB329).

## References

- 1 M. Escudero-Escribano, K. D. Jensen and A. W. Jensen, Recent advances in bimetallic electrocatalysts for oxygen reduction: design principles, structure-function relations and active phase elucidation, *Curr. Opin. Electrochem.*, 2018, **8**, 135–146.
- 2 X. Huang, Z. Zhao, L. Cao, Y. Chen, E. Zhu, Z. Lin, M. Li, A. Yan, A. Zettl, Y. M. Wang, X. Duan, T. Mueller and Y. Huang, High-performance transition metal-doped Pt<sub>3</sub>Ni octahedra for oxygen reduction reaction, *Science*, 2015, **348**, 1230–1234.
- 3 L. Zhang, R. Iyyamperumal, D. F. Yancey, R. M. Crooks and G. Henkelman, Design of Pt-shell nanoparticles with alloy cores for the oxygen reduction reaction, *ACS Nano*, 2013, **7**, 9168–9172.
- 4 J. Choi, J. Cho, C. W. Roh, B. S. Kim, M. S. Choi, H. Jeong, H. C. Ham and H. Lee, Au-doped PtCo/C catalyst preventing Co leaching for proton exchange membrane fuel cells, *Appl. Catal., B*, 2019, **247**, 142–149.
- 5 G. N. Derry and R. Wan, Comparison of surface structure and segregation in AgAu and NiPd alloys, *Surf. Sci.*, 2004, **566**–**568**, 862–868.
- 6 L. Zhang, Z. Dong, S. Wang and L. Luo, Gas adsorbate-induced Au atomic segregation and clustering from Cu(Au), *Sci. China Mater.*, 2021, **64**, 1256–1266.
- 7 K. Liu, S. Zhang, D. Wu, L. Luo, X. Sun, X. Chen, D. Zakharov, S. Cheng, Y. Zhu, J. C. Yang, G. Wang and G. Zhou, Effect of surface steps on chemical ordering in the subsurface of Cu(Au) solid solutions, *Phys. Rev. B*, 2021, **103**, 1–9.
- 8 H. Reichert, P. Eng, H. Dosch and I. Robinson, Thermodynamics of Surface Segregation Profiles at Cu<sub>3</sub>Au(001) Resolved by X-Ray Scattering, *Phys. Rev. Lett.*, 1995, **74**, 2006–2009.
- 9 X. Liu, P. Zou, L. Song, B. Zang, B. Yao, W. Xu, F. Li, J. Schroers, J. Huo and J. Q. Wang, Combinatorial High-Throughput Methods for Designing Hydrogen Evolution Reaction Catalysts, *ACS Catal.*, 2022, **12**, 3789–3796.
- 10 J. Luyten, S. Helfensteyn and C. Creemers, Segregation in ternary alloys: an interplay of driving forces, *Appl. Surf. Sci.*, 2003, **212**–**213**, 833–838.



- 11 P. Wynblatt and A. Landa, Computer simulation of surface segregation in ternary alloys, *Comput. Mater. Sci.*, 1999, **15**, 250–263.
- 12 E. V. Levchenko, A. V. Evteev, R. Kozubski, I. V. Belova and G. E. Murch, Molecular dynamics simulation of surface segregation in a (110) B2-NiAl thin film, *Phys. Chem. Chem. Phys.*, 2011, **13**, 1214–1221.
- 13 B. Zhang, T. Edmund, X. Shu, W. Hu and H. Deng, Simulation calculations of surface segregation for Au-Cu alloys using an analytic embedded atom model, *Phys. Status Solidi A*, 2005, **202**, 2686–2699.
- 14 S. M. Aspera, R. L. Arevalo, H. Nakanishi and H. Kasai, First principles study of surface stability and segregation of PdRuRh ternary metal alloy system, *Surf. Sci.*, 2018, **671**, 51–59.
- 15 Y. Yang, Z. Guo, A. J. Gellman and J. R. Kitchin, Simulating Segregation in a Ternary Cu-Pd-Au Alloy with Density Functional Theory, Machine Learning, and Monte Carlo Simulations, *J. Phys. Chem. C*, 2022, **126**, 1800–1808.
- 16 H. S. Pillai, Y. Li, S. H. Wang, N. Omidvar, Q. Mu, L. E. K. Achenie, F. Abild-Pedersen, J. Yang, G. Wu and H. Xin, Interpretable design of Ir-free trimetallic electrocatalysts for ammonia oxidation with graph neural networks, *Nat. Commun.*, 2023, **14**, 1–11.
- 17 X. Niu, S. Li, Z. Zhang, H. Duan, R. Zhang, J. Li and L. Zhang, Accelerated Optimization of Compositions and Chemical Ordering for Bimetallic Alloy Catalysts Using Bayesian Learning, *ACS Catal.*, 2025, 4374–4383.
- 18 J. Luyten and C. Creemers, Surface segregation in ternary Pt-Pd-Rh alloys studied with Monte Carlo simulations and the modified embedded atom method, *Surf. Sci.*, 2008, **602**, 2491–2495.
- 19 J. K. Nørskov, J. Rossmeisl, A. Logadottir, L. Lindqvist, J. R. Kitchin, T. Bligaard and H. Jónsson, Origin of the overpotential for oxygen reduction at a fuel-cell cathode, *J. Phys. Chem. B*, 2004, **108**, 17886–17892.
- 20 Z. L. Wang, D. Xu, J. J. Xu and X. B. Zhang, Oxygen electrocatalysts in metal-air batteries: From aqueous to nonaqueous electrolytes, *Chem. Soc. Rev.*, 2014, **43**, 7746–7786.
- 21 F. Cheng and J. Chen, Metal-air batteries: From oxygen reduction electrochemistry to cathode catalysts, *Chem. Soc. Rev.*, 2012, **41**, 2172–2192.
- 22 M. K. Debe, Electrocatalyst approaches and challenges for automotive fuel cells, *Nature*, 2012, **486**, 43–51.
- 23 A. Kulkarni, S. Siahrostami, A. Patel and J. K. Nørskov, Understanding Catalytic Activity Trends in the Oxygen Reduction Reaction, *Chem. Rev.*, 2018, **118**, 2302–2312.
- 24 C. Yu, S. Liao and H. Deng, The Rh influence on the surface distribution of the ternary alloy Pt-Pd-Rh, *Appl. Surf. Sci.*, 2007, **253**, 6074–6079.
- 25 J. Greeley, I. E. L. Stephens, A. S. Bondarenko, T. P. Johansson, H. A. Hansen, T. F. Jaramillo, J. Rossmeisl, I. Chorkendorff and J. K. Nørskov, Alloys of platinum and early transition metals as oxygen reduction electrocatalysts, *Nat. Chem.*, 2009, **1**, 552–556.
- 26 G. H. Han, S. H. Lee, S. Y. Hwang and K. Y. Lee, Advanced Development Strategy of Nano Catalyst and DFT Calculations for Direct Synthesis of Hydrogen Peroxide, *Adv. Energy Mater.*, 2021, **11**, 1–33.
- 27 S. Back, J. Na and Z. W. Ulissi, Efficient Discovery of Active, Selective, and Stable Catalysts for Electrochemical H<sub>2</sub>O<sub>2</sub> Synthesis through Active Motif Screening, *ACS Catal.*, 2021, **11**, 2483–2491.
- 28 Y. Nakaya and S. Furukawa, Catalysis of Alloys: Classification, Principles, and Design for a Variety of Materials and Reactions, *Chem. Rev.*, 2023, **123**, 5859–5947.
- 29 M. Krajčí and J. Hafner, Intermetallic Compounds as Selective Heterogeneous Catalysts: Insights from DFT, *ChemCatChem*, 2016, **8**, 34–48.
- 30 Q. Shao, F. Li, Y. Chen and X. Huang, The Advanced Designs of High-Performance Platinum-Based Electrocatalysts: Recent Progresses and Challenges, *Adv. Mater. Interfaces*, 2018, **5**, 1–24.
- 31 K. Tran and Z. W. Ulissi, Active learning across intermetallics to guide discovery of electrocatalysts for CO<sub>2</sub> reduction and H<sub>2</sub> evolution, *Nat. Catal.*, 2018, **1**, 696–703.
- 32 G. Cao, S. Yang, J. C. Ren and W. Liu, Electronic descriptors for designing high-entropy alloy electrocatalysts by leveraging local chemical environments, *Nat. Commun.*, 2025, **16**, 1251.
- 33 H. H. Kristoffersen and J. Rossmeisl, Local Order in AgAuCuPdPt High-Entropy Alloy Surfaces, *J. Phys. Chem. C*, 2022, **126**, 6782–6790.
- 34 M. Hua, X. Tian, S. Li, A. Shao and X. Lin, Theoretical design of platinum-silver single atom alloy catalysts with CO adsorbate-induced surface structures, *Phys. Chem. Chem. Phys.*, 2022, **24**, 19488–19501.
- 35 M. Hua, X. Tian, S. Li, X. Zhang, A. Shao, L. Song and X. Lin, A casting combined quenching strategy to prepare PdAg single atom alloys designed using the cluster expansion combined Monte Carlo method, *Phys. Chem. Chem. Phys.*, 2022, **24**, 2251–2264.
- 36 M. Hua, X. Tian, S. Li and X. Lin, PdAg/Ag(111) Surface Alloys: A Highly Efficient Catalyst of Oxygen Reduction Reaction, *Nanomaterials*, 2022, **12**, 1802.
- 37 G. Kresse and J. Furthmüller, Efficiency of ab-initio total energy calculations for metals and semiconductors using a plane-wave basis set, *Comput. Mater. Sci.*, 1996, **6**, 15–50.
- 38 D. Joubert, From ultrasoft pseudopotentials to the projector augmented-wave method, *Phys. Rev. B: Condens. Matter Mater. Phys.*, 1999, **59**, 1758–1775.
- 39 B. Hammer, L. B. Hansen and J. K. Nørskov, Improved adsorption energetics within density-functional theory using revised Perdew-Burke-Ernzerhof functionals, *Phys. Rev. B: Condens. Matter Mater. Phys.*, 1999, **59**, 7413–7421.
- 40 J. P. Perdew, K. Burke and M. Ernzerhof, Generalized gradient approximation made simple, *Phys. Rev. Lett.*, 1996, **77**, 3865–3868.
- 41 J. A. Zamora Zeledón, M. B. Stevens, G. T. K. K. Gunasooriya, A. Gallo, A. T. Landers, M. E. Kreider, C. Hahn, J. K. Nørskov and T. F. Jaramillo, Tuning the electronic structure of Ag-Pd





- alloys to enhance performance for alkaline oxygen reduction, *Nat. Commun.*, 2021, **12**, 1–9.
- 42 L. A. Mancera, R. J. Behm and A. Groß, Structure and local reactivity of PdAg/Pd(111) surface alloys, *Phys. Chem. Chem. Phys.*, 2013, **15**, 1497–1508.
- 43 K. M. Schüttler, L. A. Mancera, T. Diemant, A. Groß and R. J. Behm, Interaction of CO with PtAg<sub>1-x</sub>/Pt(111) surface alloys: More than dilution by Ag atoms, *Surf. Sci.*, 2016, **650**, 237–254.
- 44 A. Van de Walle, M. Asta and G. Ceder, The alloy theoretic automated toolkit: A user guide, *CALPHAD: Comput. Coupling Phase Diagrams Thermochem.*, 2002, **26**, 539–553.
- 45 L. Bengtsson, Dipole correction for surface supercell calculations, *Phys. Rev. B: Condens. Matter Mater. Phys.*, 1999, **59**, 12301–12304.
- 46 Y. Yu, W. Xiao, J. Wang and L. Wang, Understanding the surface segregation behavior of transition metals on Ni(111): A first-principles study, *Phys. Chem. Chem. Phys.*, 2016, **18**, 26616–26622.
- 47 A. D. Sison, M. M. N. A. Quaynor, S. A. K. Navodye and G. T. K. K. Gunasooriya, Insights into Segregation and Aggregation in Dilute Atom Alloy Catalysts Using DFT and Machine Learning, *ChemCatChem*, 2025, **8**, 1–14.
- 48 M. H. F. Sluiter and Y. Kawazoe, Invariance of truncated cluster expansions for first-principles alloy thermodynamics, *Phys. Rev. B: Condens. Matter Mater. Phys.*, 2005, **71**, 1–2.
- 49 A. van de Walle and G. Ceder, Automating first-principles phase diagram calculations, *J. Phase Equilib.*, 2002, **23**, 348–359.
- 50 D. B. Laks, L. G. Ferreira, S. Froyen and A. Zunger, Efficient cluster expansion for substitutional systems, *Phys. Rev. B: Condens. Matter Mater. Phys.*, 1992, **46**, 12587–12605.
- 51 J. Brorsson, Y. Zhang, A. E. C. Palmqvist and P. Erhart, Order-Disorder Transition in Inorganic Clathrates Controls Electrical Transport Properties, *Chem. Mater.*, 2021, **33**, 4500–4509.
- 52 A. van de Walle, Multicomponent multisublattice alloys, nonconfigurational entropy and other additions to the Alloy Theoretic Automated Toolkit, *CALPHAD: Comput. Coupling Phase Diagrams Thermochem.*, 2009, **33**, 266–278.
- 53 X. Xu and H. Jiang, Anion order in perovskite oxynitrides AMO<sub>2</sub>N (A = Ba, Sr, Ca; M = Ta, Nb): A first-principles based investigation, *RSC Adv.*, 2020, **10**, 24410–24418.
- 54 K. G. Papanikolaou, M. T. Darby and M. Stamatakis, CO-Induced Aggregation and Segregation of Highly Dilute Alloys: A Density Functional Theory Study, *J. Phys. Chem. C*, 2019, **123**, 9128–9138.
- 55 D. A. Patel, P. L. Kress, L. A. Cramer, A. M. Larson and E. C. H. Sykes, Elucidating the composition of PtAg surface alloys with atomic-scale imaging and spectroscopy, *J. Chem. Phys.*, 2019, **151**, 164705.
- 56 R. T. Hannagan, G. Giannakakis, R. Réocreux, J. Schumann, J. Finzel, Y. Wang, A. Michaelides, P. Deslahra, P. Christopher, M. Flytzani-Stephanopoulos, M. Stamatakis and E. C. H. Sykes, First-principles design of a single-atom-alloy propane dehydrogenation catalyst, *Science*, 2021, **372**, 1444–1447.

